JOURNAL OF PROPULSION AND POWER
Vol. 30, No. 3, May–June 2014

Initial Performance Evaluation of a Gridded Radio Frequency Ion Thruster

Logan T. Williams* and Mitchell L. R. Walker†
Georgia Institute of Technology, Atlanta, Georgia 30332

DOI: 10.2514/1.B35018

Helicon plasma sources are devices that are capable of efficiently producing high-density plasmas. There is growing interest in using a helicon plasma source in space propulsion as a replacement to the direct current plasma discharge in ion engines. A radio frequency ion engine is developed that combines a helicon plasma source with electrostatic grids and a magnetically shielded anode. Thruster performance evaluation includes estimation of the discharge plasma ion density and electron temperature and measurement of the plume current density, grid currents, and thrust. The radio frequency ion engine is tested across the following operating parameter ranges: 343–600 W radio frequency power, 50–250 G magnetic field strength, 1.0–2.0 mg/s argon flow rate, and 100–600 V discharge voltage range at an operating pressure of 1.6×10^{-5} torr Ar., discharge ion density and electron temperature range $1.5–9.3 \times 10^{16}$ m^{-3} and 5.4–9.9 eV, respectively. Maximum beam current extracted is 120 mA at a 600 V discharge and is primarily limited by ion impingement on the grids due to insufficient grid potentials. The maximum measured thrust is 2.77 mN with an average uncertainty of ±3.6 mN. Further optimization of the thruster operating conditions and grid assembly can improve thruster performance.

Nomenclature

A_a	=	anode area, m^2
B	=	magnetic flux density, T
d_s	=	screen grid aperture diameter, m
e	=	charge of an electron, C
I_A	=	accelerator grid current, A
I_a	=	anode current, A
I_b	=	beam current, A
I_s	=	screen grid current, A
I_{sat}	=	ion saturation current, A
j	=	current density, A m^{-2}
j_e	=	electron current density, A m^{-2}
$j_{e,0}$	=	electron current density at zero screen grid bias, A m^{-2}
j_i	=	ion current density, A m^{-2}
k_b	=	Boltzmann's constant, m^2 kg s^{-2}
l_e	=	effective sheath length, m
m_e	=	electron mass, kg
m_i	=	ion mass, kg
N_a	=	number of grid apertures
n_0	=	bulk plasma ion number density, m^{-3}
P_{norm}	=	normalized perveance, A V$^{-3/2}$
p_b	=	base pressure, torr
p_g	=	ion gauge pressure, torr
p_o	=	operating pressure, torr
T_e	=	electron temperature, eV
V_b	=	beam voltage, V
V_{ctg}	=	cathode-to-ground voltage, V
V_D	=	discharge voltage, V
V_f	=	floating potential, V
V_s	=	screen grid potential, V
$v_\perp$	=	velocity orthogonal to magnetic field line, m · s^{-1}
α_d	=	90% divergence half-angle, deg
γ	=	beam divergence factor
μ	=	magnetic moment, kg m^2 s^{-2} T^{-1}
φ_s	=	sheath potential, V
χ	=	gas correction factor

Received 10 April 2013; revision received 1 December 2013; accepted for publication 20 December 2013; published online 21 April 2014.

*Graduate Research Assistant, Aerospace Engineering, High-Power Electric Propulsion Laboratory; lwilliams@gatech.edu. Student Member AIAA.

†Associate Professor, Aerospace Engineering, High-Power Electric Propulsion Laboratory; mitchell.walker@ae.gatech.edu. Associate Fellow AIAA.

I. Introduction

A HELICON plasma source is a highly efficient device capable of creating a high-density, low-temperature plasma using RF waves transmitted from an antenna [1–7]. Radial Trivelpiece-Gould waves couple to the helicon wave that propagates through a plasma, depositing energy into the plasma. The RF energy is deposited into the free plasma electrons, creating an energy distribution within the electron population. The electron energy distribution function can be manipulated by changing the operational parameters, such as RF power, RF frequency, and applied dc magnetic field strength. Electron-neutral collisions where the electrons have energy exceeding the neutral atom ionization energy result in the creation of an ion–electron pair.

A helicon thruster is a device that uses a helicon source to create and accelerate ions. There are two approaches to helicon thrusters: a single stage device that creates and accelerates ions simultaneously or a two-stage device that separates ionization and ion acceleration. Most attempts to create a helicon thruster have focused on the single-stage approach [8–18]. The advantage to this configuration is that it has no electrode exposed to the plasma and thus erosion, which is one of the primary lifetime determining factors, is greatly mitigated. The problem with this thruster design is that most devices have been characterized by a few millinewtons of thrust and efficiency below 3% [15–18]. One notable exception to this is the first stage of the Variable Specific Impulse Magnetoplasmadynamic Rocket, where the thrust of the helicon stage of the VX-100 was estimated to be approximately 0.4 N [19]. However, this occurred at a much higher power level and, at the reported operating conditions, had an approximate efficiency of 2%. Because the helicon plasma source has a high efficiency, the low thrust efficiency is likely created in the ion acceleration stage of the helicon thruster. This is further supported by work on the helicon stage of the VX-200 only reporting a drop in plasma potential of approximately 10 V [20].

In addition to the helicon propulsion research focused on the helicon source as the entire thruster, there has been some investigation into two-stage helicon thrusters that use an additional ion accelerator used in conjunction with a helicon source. Early experiments were not direct propulsion research, but instead focused on ion

beam generation for general application, such as plasma processing, using single aperture setups [21–23]. Recently, there has been development of thruster systems that combine the helicon plasma source with an additional acceleration stage for the explicit purpose of thrust generation [24,25]. By separating the ion generation and the ion acceleration mechanisms, the two-stage design potentially preserves the high ionization efficiency of the helicon source and avoids the low efficiency apparent in most helicon thrusters. As an example of a two-stage dc engine, the NSTAR ion engine demonstrated a thrust-to-power ratio of 40.5 mN/kW, a specific impulse of 3127 s, and an efficiency of 61% [26]. A greater degree of development has been done for two-stage engines that use an inductive RF discharge instead of a helicon discharge [27–29]. One such engine, the RIT-35, is capable of a thrust-to-power ratio of 35.1 mN/kW, a specific impulse of 3190 s, and an efficiency of 72.5% [29]. However, research into application of a helicon plasma source in a two-stage thruster design remains limited.

This work presents the initial performance of a nominal gridded helicon ion thruster (GHIT) that combines the helicon plasma source with electrostatic grids used in ion engines. As is later discussed in Sec. III.A, because the device has not been conclusively confirmed to operate in a helicon mode, it cannot be definitively called a helicon thruster; however, throughout the rest of the paper, the thruster is referred to by the nominal acronym to distinguish it from a Radio frequency Ion Thruster (RIT) due to the distinct design. This design uses a magnetically shielded anode to bias the discharge plasma potential and electrostatic grids to accelerate the ions, all while using the axial dc magnetic field found in helicon plasma sources. Performance metrics of interest are the discharge plasma ion density and electron temperature, beam divergence angle, and extracted beam current. The GHIT is evaluated over a range of operating conditions: 343–600 W RF power, 50–250 G magnetic field strength, 1.0–2.0 mg/s argon flow rate, and 100–600 V discharge voltage range.

II. Experimental Apparatus

A. Vacuum Facilities

All experiments were conducted in vacuum test facility 1 (VTF-1). VTF-1 is a stainless steel vacuum chamber 4 m in diameter with a length of 7 m. Two 3800 ft^3/min blowers and two 495 ft^3/min rotary-vane pumps evacuate the chamber to a moderate vacuum (about 30 mtorr). High vacuum is normally reached by using six 48 in. diffusion pumps with a cosmbined pumping speed of 485,000 l/s on argon. Because of the presence of optical baffles, the effective pumping speed is 125,000 l/s. The chamber pressure is measured with a BA-571 ion gauge connected to a Varian SenTorr controller with an uncertainty of 20%. An MKS-type 247 four-channel readout in conjunction with an MKS 1179 mass flow controller regulates the gas flow into the helicon with an error of $\pm 1\%$ [30]. The base pressure of VTF-1 for these experiments is 1.5×10^{-5} torr. Figure 1 shows a schematic of the VTF.

The operating pressure p_o is derived by a correction of the pressure measured by the ion gauge, given by

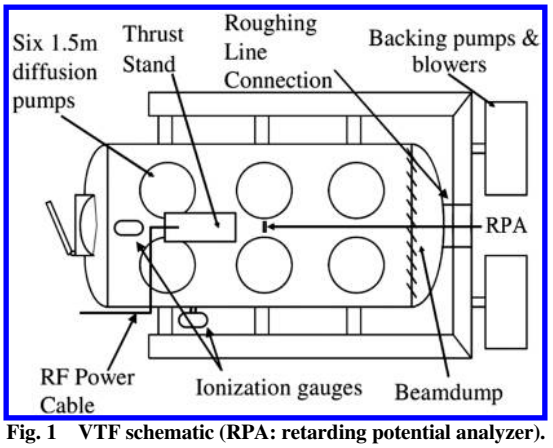

Fig. 1 VTF schematic (RPA: retarding potential analyzer).

$$p_o = \frac{p_g - p_b}{\chi} + p_b \tag{1}$$

where p_g is the pressure given by the ion gauge, p_b is the base pressure, and χ is the gas correction factor, which is 1.29 for argon.

B. Gridded Helicon Ion Engine

There are three subsystems to the GHIT: the helicon plasma source, the electrostatic grid assembly, and the thruster discharge circuit. The helicon discharge serves to ionize the propellant, the grid assembly extracts the ions from the discharge chamber, and the discharge circuit, which contains an anode inside the helicon discharge and an external cathode, biases the discharge plasma to create a net potential drop to accelerate the ions and extracts electrons to neutralize the beam. All components are electrically isolated from the chamber, and the magnetic coils are isolated from the thrust stand using polyether ether ketone (PEEK) spacers. Figure 2 shows the configuration of the thruster.

1. *Helicon Plasma Source*

The helicon plasma source consists of a Pyrex discharge chamber 27.3 cm long and 14.0 cm in diameter. The axial magnetic field is provided by two 725-turn solenoids 7.6 cm wide with a 19.7 cm inner diameter. The solenoids are placed 10.2 cm apart. Figures 3 and 4 show the helicon source geometry and the on-axis magnetic field strength for the five solenoid currents used, respectively. The magnetic field strengths are referred to by the strength at the center of the antenna; thus, although the device is tested at solenoid currents of 1.26, 2.51, 3.76, 5.01, and 6.26 A, it is referred to as 50, 100, 150, 200, and 250 G, respectively.

The antenna used is a double saddle antenna, 20.3 cm long and 15.9 cm in diameter and is driven at 13.56 MHz. The antenna is

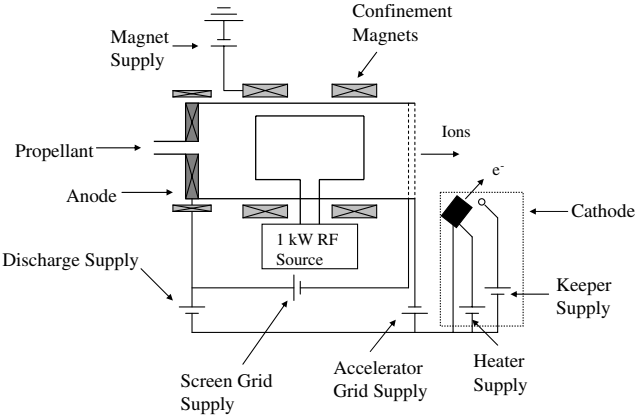

Fig. 2 GHIT configuration.

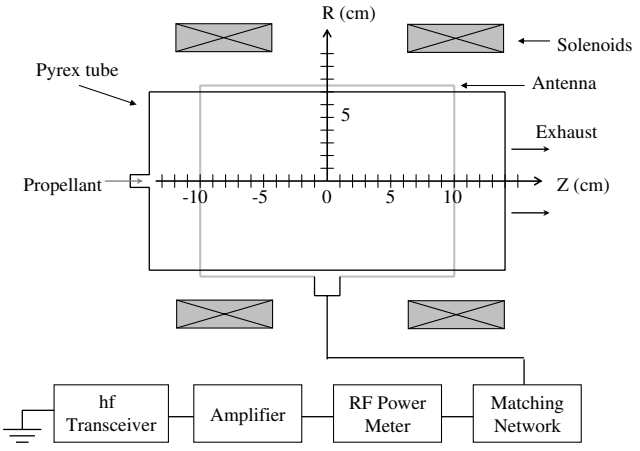

Fig. 3 Helicon configuration and RF schematic.

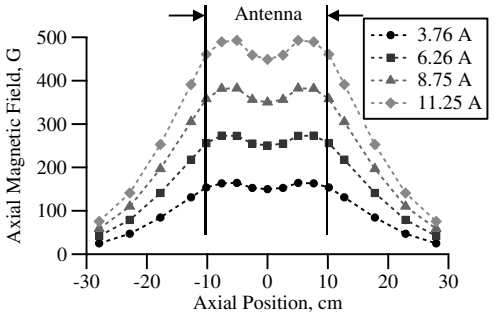

Fig. 4 Centerline axial magnetic field strength as a function of solenoid current.

composed of copper strips 1.25 cm wide and 0.318 cm thick welded together. A gap of 0.635 cm separates the two terminals; the center conductor of the coaxial cable is connected to the exhaust side terminal, and the shield is connected to the inlet side terminal. The antenna is wrapped in fiberglass tape to prevent direct electrical contact between the antenna and any stray plasma or the solenoids. A transmission line of RG-393 with a total length of 6.9 m connects the matching network to the feedthrough and then to the antenna. The outer shield of the feedthrough is grounded to the chamber. The RF system is grounded using a 0.5-in.-diam rod, 6 ft long, driven into the ground. Figure 5 shows a CAD model of the antenna.

2. *Grid Assembly*

The grid assembly consists of two stainless steel grids, the screen and accelerator (accel), and an insulated support structure that maintains a set separation between the grids. The screen grid aperture diameter is 1.5 mm, with the accel grid aperture diameter 1.2 mm. The grid thickness is 0.635 mm and the grid separation distance is 1.0 mm. Both grids are laser cut from SS 316 with the apertures arranged in a 60 deg hexagonal pattern with a pitch of 1.75 mm.

The grid assembly starts with a base piece fabricated from PEEK sized to fit on the end of the discharge chamber. The screen grid is mounted on the base where four protrusions extend from the base and fit into side holes of the grid to restrict rotational motion of the grid. An imbedded aluminum electrode allows connection to the screen grid through the side of the base. Two 0.5-mm-thick mica rings are placed on top of the screen grid to maintain the designed 1.0 mm grid separation distance. The accel grid is set within a PEEK holder that contains protrusions similar to the base for the same reason. The PEEK holder also has two protrusions on the side that match two recessions on the final piece, the grid press. The grid press is also fabricated from PEEK and bolts to the base part. The grid press serves two functions: 16 set screws compress the grid stack together, and the grid press covers the sides of the grids, preventing arcing around the mica. The combination of the nested protrusions maintains aperture alignment. One of the set screws is aligned with a hole in the accel grid holder that allows electrical contact to the accel grid. Four screws mount the entire assembly to the discharge chamber. Figure 6 shows an exploded CAD view of the grid assembly.

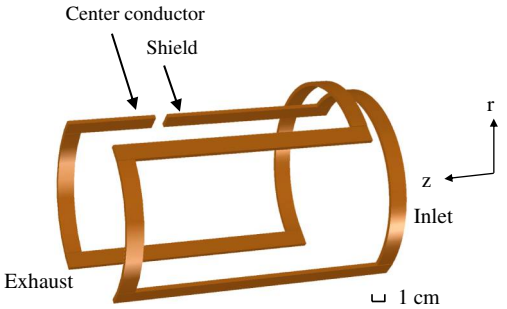

Fig. 5 CAD model of the double saddle antenna. Arrows indicate coaxial connection terminals.

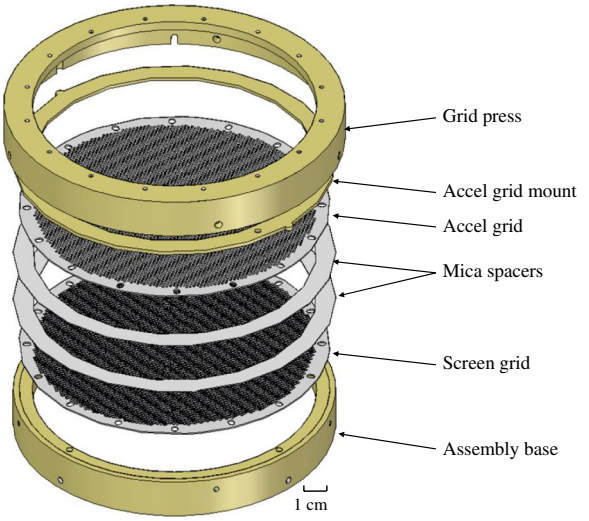

Fig. 6 Exploded view of the grid assembly.

3. *Thruster Discharge Circuit*

The final subsystem is the thruster discharge circuit, which consists of an anode placed inside the discharge chamber and a cathode mounted downstream of the grid assembly. The thruster discharge circuit serves two functions. The first is to bias the plasma potential within the discharge chamber. The net energy of the ions leaving the thruster is determined not by the potential drop across the grids, but by the net potential drop between the discharge plasma and the space potential. The potential drop between the grids only determines the maximum current density that can pass through the grids. Even if the acceleration grid provides a steep drop in potential, the ions would have to come back up the potential hill to end at the space potential. Thus, the anode is required to push the potential of the discharge plasma above the space potential so that a net potential exists to accelerate the ions.

The second purpose of the thruster discharge circuit is to provide a current path between the neutralizer cathode and the discharge plasma. As ions exit the discharge chamber, they leave behind their corresponding electrons; if left unchecked, this would create a buildup of negative charge in the discharge chamber. Thus, by including the anode and connecting it to the neutralizer cathode, the excess electrons can be collected and used to neutralize the ion plume.

The anode is a 6.5-mm-thick stainless steel 316 disk with a 13.85 cm outer diameter placed at the inlet side of the interior of the discharge chamber. A 1.59-mm-diam, 25-mm-long stainless steel rod is welded to the back of the anode and extends through a sealed hole in the back of the discharge chamber to allow for an electrical connection to the anode. The location of the anode places it 3 cm upstream from the edge of the antenna, which raises the possibility of power coupling to the discharge supply. To reduce RF pickup by the anode, the line connecting the anode to the discharge supply is wrapped around a NiZn ferrite toroid, which provides approximately 300 Ω of impedance at 13.56 MHz. The same setup is also used for the lines connecting the screen grid and accel grid.

An additional solenoid was added to examine the effects of providing a magnetic barrier to the anode. Ideally, the presence of a magnetic barrier should increase the electron energy required to reach the anode, which would increase the electron temperature of the discharge plasma. This in turn would increase the Bohm velocity of the ions into the grid sheath and thus the extracted ion current. The magnetic barrier is designed to be a one-sided magnetic mirror that increases the axial magnetic field strength near the anode. The additional solenoid is 525 turns with an inner diameter of 17 cm and is aligned with the previous two solenoids. The new solenoid is placed at the rear of discharge chamber such that the center of the anode coincides with the center of the solenoid.

The cathode is an in-house fabricated lanthanum hexaboride (LaB_6) hollow cathode following the design of the Moscow Aviation

Institute. The cathode consists of a pellet of LaB_6 as the electron emissive material placed in a molybdenum holder. A coil of tungsten is wrapped into a helical spring to fix the LaB_6 in place while also serving as the heater. A thin sheet of molybdenum is bent to form a cylindrical radiation shield that extends along the length of the heater coil. The radiation shield serves two purposes: It reduces radiation losses from the heater coil and acts as an electrical connection between the heater coil and the heater connection rod that extends out the back of the cathode. Ceramic spacers fix the position of the radiation shield and heater connection relative to a center threaded rod that serves as a common cathode connection. The center assembly then fits inside a titanium shell with molybdenum foil wrapped around it, and a tantalum disk with a center bore is placed in front of the pellet; these both serve as thermal insulation to prevent the titanium shell from melting. Once the LaB_6 pellet reaches its operating temperature, it emits electrons; by flowing a gas through the cathode, the number of electrons emitted is increased by secondary emission via collisions of the primary electrons into the neutral atoms. An extraction wire called a keeper is placed just past the center orifice to aid in electron generation. A schematic of the cathode is shown in Fig. 7.

4. *Thruster Circuit Measurement*

The thruster circuit is shown in Fig. 2. The discharge plasma is treated as a conductive element that connects the grids and the anode. The anode is assumed to collect a net current of electrons, which results in a positive current into the discharge. The grids are assumed to collect only ions and thus are depicted as positive currents out of the discharge. Any ion current that is not collected by either the screen or the accel grid is assumed to enter the plume as part of the ion beam. This ion current must be neutralized by an electron current of equal magnitude from the cathode, which is connected to the discharge supply. This electron current is represented as a positive current flowing to the discharge supply from the cathode. The individual currents collected by the anode and the grids are determined by measuring the voltage across three resistor shunts. The resistances of the shunts for the anode, screen grid, and accel grid, as measured by an Agilent U1733C RLC meter, are 5.085, 5.095, and 5.079 Ω, respectively. Figure 8 shows the thruster circuit. It should be noted that, although the screen and accel grids are biased below the anode and cathode, respectively, they are reported by their magnitudes.

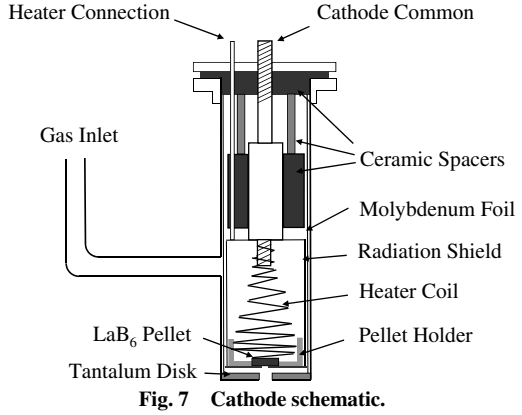

Fig. 7 Cathode schematic.

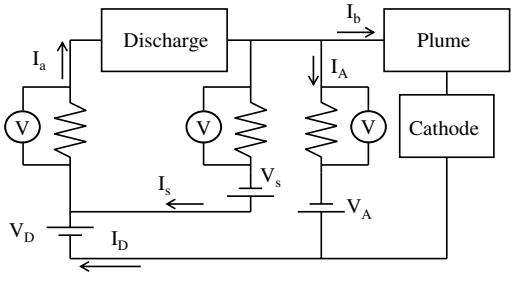

Fig. 8 GHIT thruster circuit.

Because the discharge plasma in the steady state must have charge neutrality, the beam current I_b can be defined from Fig. 8 as

$$I_b = I_a - I_s - I_A \tag{2}$$

where I_a is the anode current, I_s is the screen grid current, and I_A is the accel grid current. The voltage across the resistor shunts are measured using three Fluke 83 V multimeters. The Fluke 83 V has an uncertainty of ±0.3% of the measured value for the measurement range used. The shunt resistance is measured with an Agilent U1733C RLC meter with an accuracy of $\pm 0.7\% + 0.008\ \Omega$ for the 20 Ω range used. The total uncertainty of the current measurements is ±0.9%. The anode and grid potentials are supplied by a TopCon Quadro 1000 V, 20 A, and two Lambda EMI GEN600-2.6E power supplies, respectively.

C. Faraday Probe

A Jet Propulsion Laboratory-style Faraday probe was used to measure the ion current density in the plume of the thruster [31–37]. The primary function of the Faraday probe is to measure the ion current density as a function of angular position along a circular arc centered on the exit plane of the thruster. The shape of the plasma plume is quantified by the beam divergence half-angle, the angle from the center of the plume that captures 90% of the ion beam current. Ideally, the divergence angle should be as small as possible because this signifies a highly collimated beam where minimal ion energy is spent on radial motion and axial velocity is maximized.

A Faraday probe consists of two primary elements: a collector and a guard ring. The collector is biased negatively to repel electrons, which ensures that the current collected by the probe is solely due to ions and not reduced by a partial electron collection. The collector is a tungsten-coated aluminum disk, 22.4 mm in diameter and 6.05 mm thick. The guard ring is 25.2 mm in outer diameter with a thickness of 0.75 mm and is 5.52 cm long. A threaded rod is attached to the back of the collector and passes through the back of the probe, serving as the electrical connection. Inside the probe, the threaded rod is separated from the guard ring by a ceramic spacer. Figure 9 shows a schematic of the probe. The probe is operated at a bias of 30 V below chamber ground, 50 cm downstream of the exit plane of the thruster.

The total beam current can be calculated by integrating the current density across the surface area of the hemisphere [31,37]. Assuming that the plume is radially symmetric, the current density is only a function of the angle θ. The divergence half-angle α_d is arbitrarily defined as half of the sweep required to contain 90% of the beam current. Mathematically, this is stated as

$$0.9 I_b = \sum_{-\alpha_d}^{\alpha_d} 2\pi r^2 j(\theta) \sin\theta(\Delta\theta) \tag{3}$$

The beam divergence factor quantifies the lost thrust due to plume divergence. Ions are accelerated into the plume with axial and radial components to the velocity. Because of radial symmetry, the sum of the radial components of all the ions in the plume is zero and thrust is a function solely of axial ion velocity. Ions that are accelerated at larger angles from centerline thus have a smaller percentage of the energy gained from the drop in electric potential that is used for thrust. Therefore, the beam divergence factor is defined as

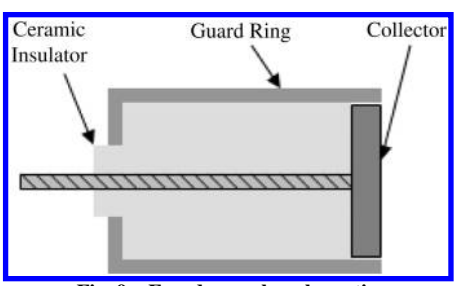

Fig. 9 Faraday probe schematic.

$$\gamma = \cos \alpha_d \tag{4}$$

D. Thrust Stand

The thrust of the helicon was measured with a null-type inverted pendulum thrust stand [38]. The thrust stand consists of two parallel plates connected by a series of four flexures that support the upper plate and allow deflection as a force is applied. A linear variable differential transformer (LVDT) measures the position of the upper plate, whereas two electromagnetic actuators control the motion. One actuator, the damper coil, compensates for vibrations, and the second, the null coil, holds the upper plate stationary. The thrust stand operates by using two proportional-integral-derivative control circuits that use the LVDT signal as input and the current through one of the actuators as the output. The resulting current through the null coil is directly correlated to the force required to maintain the position of the thrust stand and is calibrated by comparing the null coil current to the application of a series of known weights. The driving current in the null coil of the thrust stand is digitally recorded using a LabView VI interfacing with a Keithley 2410 SourceMeter at a frequency of 15 Hz. The uncertainty is calculated as the standard deviation of the measurements when the helicon is not running. The uncertainty ranges from ± 0.5 to 2.3 mN with an average value of ± 1.9 mN. A water-cooled copper shroud surrounds the thrust stand components to maintain thermal equilibrium.

E. Discharge Plasma Analysis

Two key performance metrics of an ion engine discharge chamber are the ion number density and electron temperature. The most direct method to measure these parameters is to use a Langmuir probe inside the discharge chamber, but the presence of the grids greatly increases the complexity of taking such a measurement. An alternative approach is to use the screen grid as a planar Langmuir probe to create a spatially averaged estimate of the ion number density and the electron temperature. The latter approach was used because it only required sweeping the screen grid potential and measuring the current collected by the screen grid to generate an I–V characteristic. These average values are used to quantify the behavior of the discharge at each operating condition and can be used to observe coupling mode changes in the discharge plasma.

During operation, a sheath forms between the grids and the discharge chamber plasma. If the screen grid is biased below the discharge plasma potential, only a fraction of the electron flux incident on the sheath will have sufficient energy to traverse the adverse potential gradient and reach the screen. In contrast, as long as the screen grid is biased below the plasma potential, the ion flux is independent of the potential drop through the sheath, hereafter called the sheath potential for convenience. Thus, as the screen grid potential is progressively biased below the anode potential, the ion current will be constant and the electron current will decrease. Assuming a Maxwellian electron population [39], the net current to the screen is

$$I_s = en_0 A_s \left(0.61 \left(\frac{k_b T_e}{m_i} \right)^{1/2} - \frac{1}{4} \left(\frac{8 k_b T_e}{\pi m_e} \right)^{1/2} \exp\left(\frac{e\phi_s}{k_b T_e} \right) \right) \tag{5}$$

where $j_{e,0}$ is the electron flux when the screen grid collects zero net current, and ϕ_s is the screen grid sheath potential. The screen grid sheath potential can be defined in terms of the anode sheath potential ϕ_a,

$$\phi_s = \phi_a - V_s \tag{6}$$

where V_s is the bias applied on the screen grid below ground. In Eq. (6), the screen grid bias is defined as absolute values that correspond to the set voltage on the screen grid power supply as connected in Fig. 2. At the floating potential V_f, where the screen grid collects zero net current, the anode sheath potential can be related to the electron temperature by

$$1 = 1.16 \left(\frac{m_i}{\pi m_e} \right)^{1/2} \exp\left(\frac{e(\phi_a - V_f)}{k_b T_e} \right) \tag{7}$$

The ion saturation current I_{sat} is the ion current collected by an electrode in the absence of an electron current and is the maximum current collected by the screen grid at the end of the I–V sweep. Substituting Eqs. (6) and (7) and the ion saturation current into Eq. (5) yields

$$I_s = I_{\text{sat}} \left(1 - \exp\left(\frac{-e(V_s - V_f)}{k_b T_e} \right) \right) \tag{8}$$

The electron temperature is then estimated through the use of a least-squares curve fit of the I-V sweep of the screen grid to Eq. (8).

Whereas the electron temperature can be determined from the change in screen grid current as a function of grid potential, the ion number density is found using the maximum ion current collected through a sheath. Because the ion flux incident on the sheath is equal to the Bohm current, the total ion current also requires the collection area. However, during the I–V sweeps, the accel grid potential is 100 V below cathode, much lower than is designed for full operation, and the accel grid sheath is not a full Child–Langmuir sheath, and thus does not extend into the screen grid apertures. Instead, the discharge plasma extends past the screen grid and is present on both sides of the screen grid. Therefore, the total collection area from the screen grid is unknown. Instead, the anode can be used as the measuring electrode during full operation of the engine with the accel grid biased fully at 600 V. At this condition, the sheath area at anode and at the grids is approximately equal, neglecting small variations of the grid sheath area due to the doming of the accel grid sheath through the screen grid apertures. Furthermore, the net anode electron current must equal the ion current to the grid sheath (including ions collected by the grids, as well as accelerated into the beam) to maintain charge balance. The bulk plasma ion number density is given by

$$n_0 = \frac{I_a}{0.61 e A_a} \left(\frac{m_i}{k_b T_e} \right)^{1/2} \tag{9}$$

III. Experimental Results

Performance of the GHIT is separated into three categories: discharge plasma characteristics, thruster component currents, and plume divergence. The discharge plasma characteristics, consisting of the spatially averaged ion number density and electron temperature, quantify the ion production capability across the range of operating conditions used. The thruster component currents are the ion and electron currents collected by the grids and the anode, respectively, which can be used to determine the extracted beam current and the efficacy of the ion optics. The plume divergence angle quantifies the degree of collimation of the beam and is used to calculate the beam divergence factor. Using the preceding data, the thrust contribution from the ions can be estimated and compared with measured thrust.

A. Discharge Plasma Analysis

There are four parameters that are varied to control the discharge plasma: RF power, axial magnetic field strength, propellant flow rate, and current through the anode coil. Although not every permutation of operating conditions was tested, the sample set includes variation of each parameter with all other conditions constant. Characterization of the discharge plasma is performed with the anode biased 100 V above the cathode and no potential applied to the accel grid. Figures 10–14 show the results of the discharge analysis for each operating condition. The presented uncertainty includes the accuracy of the measurements and the rms error of the curve fit used to determine the electron temperature.

Across the tested operating conditions, the ion number density ranges from 10^{16} to 10^{17} m^{-3} and the electron temperature varies between 5 and 10 eV. It is worth nothing in Fig. 10 that ion number

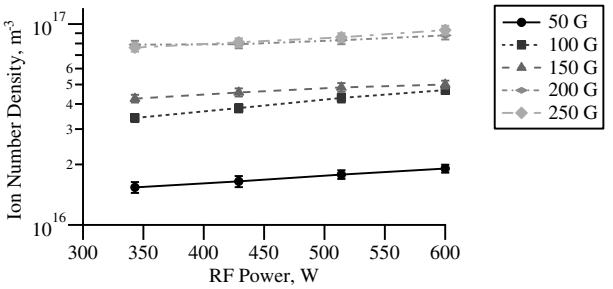

Fig. 10 Discharge ion number density as function of RF power and magnetic field; 1.5 mg/s argon, 1.6×10^{-5} torr Ar chamber pressure.

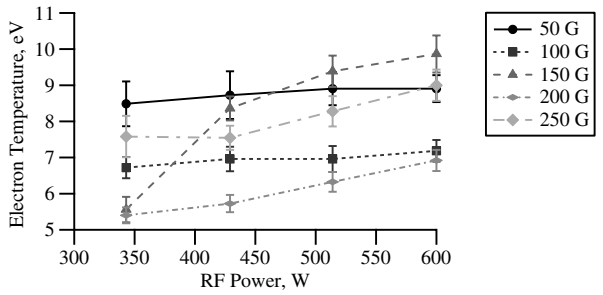

Fig. 11 Discharge electron temperature as function of RF power and magnetic field; 1.5 mg/s argon, 1.6×10^{-5} torr Ar chamber pressure.

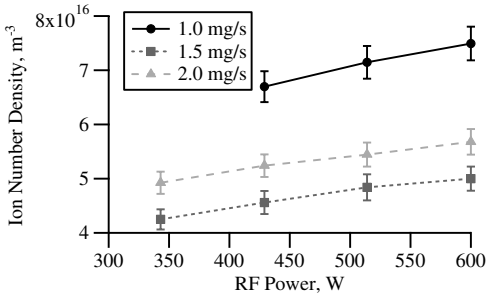

Fig. 12 Discharge ion number density as function of RF power and argon flow rate; 150 G, 1.4×10^{-5}, 1.6×10^{-5}, and 1.7×10^{-5} torr Ar chamber pressure for 1.0, 1.5, and 2.0 mg/s flow rates, respectively.

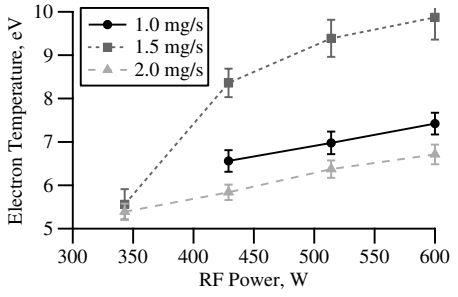

Fig. 13 Discharge electron temperature as function of RF power and argon flow rate; 150 G, 1.4×10^{-5}, 1.6×10^{-5}, and 1.7×10^{-5} torr Ar chamber pressure for 1.0, 1.5, and 2.0 mg/s flow rates, respectively.

density varies linearly with RF power with no discrete jumps that would indicate a coupling mode transition. Furthermore, rather than a linear dependence between ion number density and magnetic field strength, discrete jumps occur between 50 and 100 G, and 150 and 200 G. This behavior has been previously observed in a study of helicon plasma sources used in materials processing where the discharge chamber terminated at a conductive surface [6]. Although the antenna does not tightly restrict the excited wavelength, the presence of the grids does enforce a maximum length. As the magnetic field increases, the power deposition moves the system away from the optimal condition set by the dispersion relation until the plasma has sufficient energy to jump to the next mode. It is likely that the power range was too limited to observe a similar jump solely due to RF power. At the upper bounds of the tested power and magnetic fields, a faint blue core is observable within the discharge. This suggests that helicon mode is achieved for the 200 and 250 G, whereas operation at 50–150 G results in an inductively coupled plasma. However, the average plasma discharge parameters do not satisfy the helicon dispersion relation [40],

$$\frac{\omega}{k}\frac{\mu_0 e n_0}{B_0} = \frac{1}{a}\left[\left(\frac{ka}{\alpha_m m} + Z_m\right)^2 + k^2 a^2\right]^{1/2} \tag{10}$$

where k is the axial wave number, m is the mode number, a is the radius of the discharge chamber, and Z_m and α_m are constants from the solution of Bessel's function of the first kind. However, similar work in axially bounded helicon sources likewise do not satisfy the dispersion relation while achieving helicon mode [6,41,42]. Therefore, although the behavior of the discharge at high magnetic fields suggests helicon mode, it is still inconclusive.

The nonmonotonic behavior of the electron temperature with respect to the magnetic field supports this premise. Just after a mode transition, the plasma potential reaches a relative minimum. Because the potential drop across the sheath between the plasma discharge and the anode reflects the temperature of the electrons, this infers that electron temperature also decreases at a mode change. From Fig. 10, the proposed mode transitions would occur between 50 and 100 G, and 150 and 200 G. Thus, the magnetic fields with low electron temperatures would be 100 and 200 G, because they closely follow a mode transition, whereas 50, 150, and 250 G operation would have higher electron temperatures because the plasma is pushed away from the optimal resonance condition. This is the case in Fig. 11, where 100 and 200 G display the lowest temperatures. The relative order of each line would then be a reflection of how far that operating condition is from the point of coupling mode transition, which would suggest 150 G was furthest away the most recent mode transition.

Finally, the anode coil has the smallest effect on the discharge plasma, with a fourfold increase in magnetic field increasing the density by approximately 10%. The electron temperature is increased by a similar amount across the same range.

B. Thruster Circuit

Figure 15 shows an example breakdown of thruster circuit currents as a function of discharge voltage. For the sake of brevity, only a sample of the data is presented. Figure 16 provides an example for how the beam current varies as the discharge voltage and the RF power are changed. For all test cases, increasing either parameter increases the beam current, though the effect does not always appear as linear as the case in Fig. 16.

A useful quantifier of the performance of the ion optics is the ratio of the ion current collected by the accel grid to the beam current, called the relative accel grid current. Figure 17 shows the relative accel grid current plotted against the normalized perveance for the

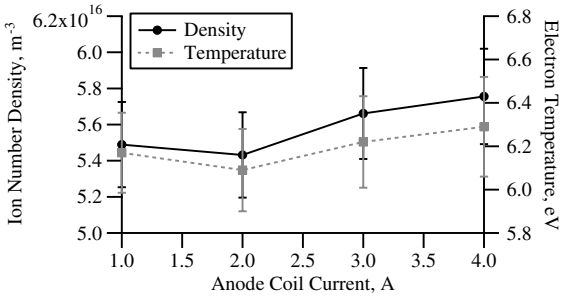

Fig. 14 Discharge ion number density and electron temperature as function of anode coil current; 500 W RF power, 150 G, 1.5 mg/s argon flow rate, 1.6×10^{-5} torr Ar chamber pressure.

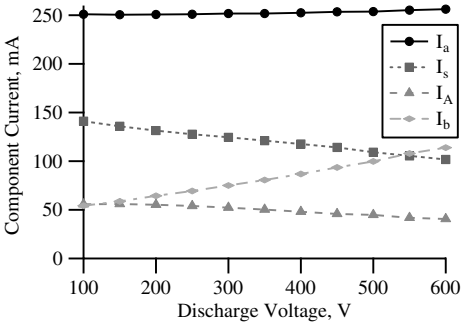

Fig. 15 Thruster circuit currents as function of discharge voltage; 600 W RF power, 100 G magnetic field, 1.5 mg/s argon, 35 V screen grid, 150 V accel grid, 1.6×10^{-5} torr Ar chamber pressure.

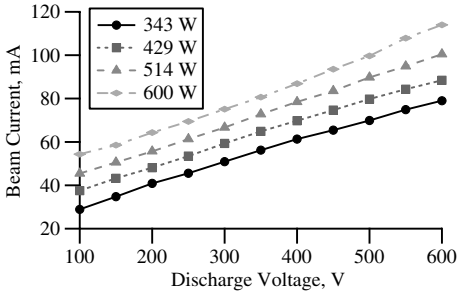

Fig. 16 Beam current as function of discharge voltage and RF power; 100 G magnetic field, 1.5 mg/s argon, 35 V screen grid bias, 150 V accel grid bias, 1.6×10^{-5} torr Ar chamber pressure.

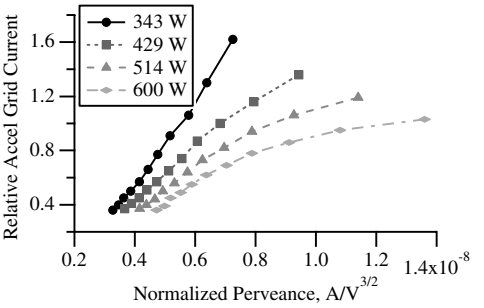

Fig. 17 Relative accel grid current as function of normalized perveance and RF power; 100 G magnetic field, 1.5 mg/s argon, 35 V screen grid bias, 150 V accel grid bias, 1.6×10^{-5} torr Ar chamber pressure.

same operating conditions used in Fig. 16. Normalized perveance is defined as

$$P_{\text{norm}} = \frac{I_b}{N_a V_T^{3/2}} \left(\frac{l_e}{d_s}\right)^2 \tag{11}$$

where N_a is the number of apertures in each grid, V_T is the total potential drop between the two grids, l_e is the effective accel grid sheath thickness, and d_s is the screen grid aperture diameter.

The first observation of Fig. 17 is the relative accel grid current is not constant for the same normalized perveance. The ion optics are determined by the placement and shape of the accel grid sheath, which is set by the perveance. Even though the discharge plasma density and temperature changes with the RF power, this would be captured in the normalized perveance as a change in beam current. The expectation is that the ion optics, represented as the ratio of extracted ions striking the accel grid to beam ions, should be constant for any given normalized perveance. However, this assumes that the perveance is normalized at each aperture, or that the discharge plasma conditions are uniform across the grids. This is unlikely to be a valid assumption, because the ion number density is likely not constant along the radius of the exit plane. The most likely explanation is that as the RF power increases, and the radial ion density and electron temperature distributions change, altering the distribution of local perveance at each aperture. The change in normalized perveance captured in Fig. 17 reflects the change in overall ion optics as the discharge plasma changes with RF power.

An example of where this effect occurs to a much smaller extent is shown in Figs. 18 and 19. In this data set, there is still variation of the beam current with RF power and discharge voltage, but the relative accel grid current as a function of normalized perveance is much more consistent. This degree of consistency for the same magnetic field strength but different RF power changes as the magnetic field strength is varied. This is more clearly seen by comparing Fig. 19 to Fig. 17. This suggests that the change in the discharge plasma density and temperature spatial distributions is a function of the magnetic field.

Further evidence of the effect of the magnetic field on the ion optics can be seen in Fig. 20, which shows the relative accel grid current for each magnetic field at 600 W. The five curves are quite disparate and show no general trend with the magnetic field. In contrast, Figs. 17 and 19 show either nearly identical shapes or a distinct similarity between lines corresponding to differing RF power. The marked difference in the response of the relative accel grid current to the two parameters shows that the magnetic field has the greater impact, whereas the RF power only slightly alters the shape of the plot, if at all. Continuing the line of thought that variance in relative accel grid current for the same grid geometry is a result of changes in the discharge plasma spatial distribution, this suggests that the magnetic field has a greater impact on shaping the discharge plasma than does RF power.

C. Beam Divergence

There are two operational parameters that are varied to determine their effects on the beam divergence: the discharge voltage and the axial magnetic field. The discharge voltage impacts the beam divergence by setting the axial kinetic energy and by altering the value of the voltage ratio R. As the discharge voltage increases, the total potential drop experienced by the ion increases, which increases the axial velocity component relative to the radial velocity component

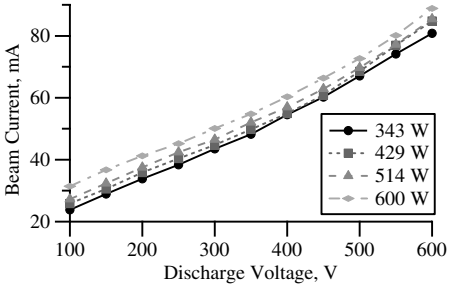

Fig. 18 Beam current as function of discharge voltage and RF power; 150 G magnetic field, 1.5 mg/s argon, 35 V screen grid bias, 150 V accel grid bias, 1.6×10^{-5} torr Ar chamber pressure.

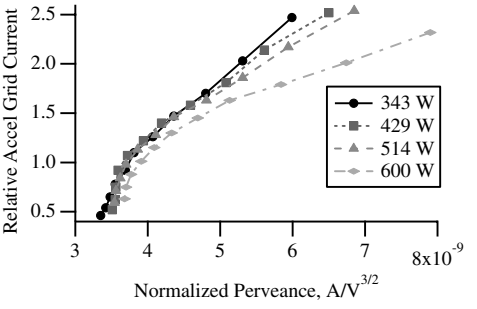

Fig. 19 Relative accel grid current as function of normalized perveance and RF power; 150 G magnetic field, 1.5 mg/s argon, 35 V screen grid bias, 150 V accel grid bias, 1.6×10^{-5} torr Ar chamber pressure.

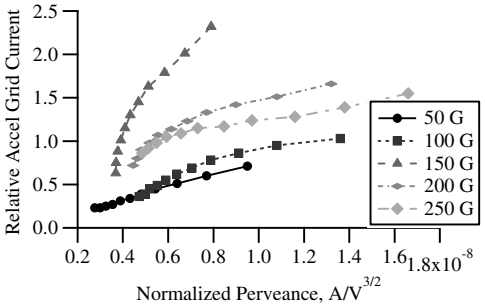

Fig. 20 Relative accel grid current as a function of normalized perveance and magnetic field; 600 W RF power, 1.5 mg/s argon, 35 V screen grid bias, 150 V accel grid bias, 1.6×10^{-5} torr Ar chamber pressure.

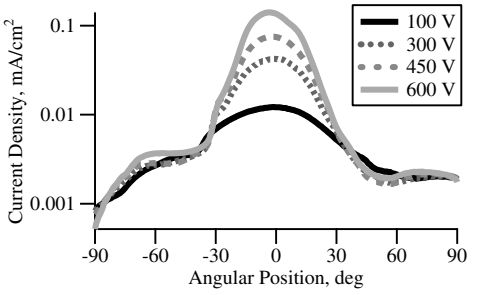

Fig. 22 Plume current density as function of discharge voltage 50 cm from grids; 429 W RF power, 150 G magnetic field, 1.5 mg/s argon, 35 V screen grid bias, 150 V accel grid bias, 1.6×10^{-5} torr Ar chamber pressure.

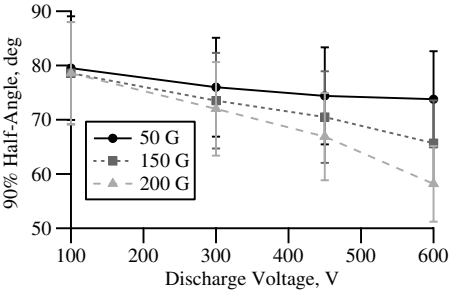

Fig. 23 Beam divergence half-angle as function of discharge voltage and magnetic field 50 cm from grids; 429 W RF power, 150 G magnetic field, 1.5 mg/s argon, 35 V screen grid bias, 150 V accel grid bias, 1.6×10^{-5} torr Ar chamber pressure.

of random thermal motion. Increasing the discharge voltage also increases R, which is the ratio of the net beam voltage to the total potential drop across the grids. Because the accel grid is biased below the cathode, as an ion exits the grids, it encounters an adverse potential gradient. Although the ions have sufficient energy to cross the gradient, the passage imparts a small radial velocity component. This effect is generally smaller than the impact of the axial kinetic energy, but still adds to divergence if not taken into account. A general rule is to keep R less than 0.8 [40].

The other parameter of interest is the axial magnetic field. Although the magnetic field is far too weak to magnetize the ions, near the grids it is still high enough to magnetize the electrons. If electrons are confined, an ambipolar electric field arises to accelerate the electrons to the ions and slow the ions. If the electrons are bound to magnetic field lines that rapidly diverge out along the radial axis, this could lead to an electric field with a radial component downstream of the grids, which could theoretically impart a radial velocity component on the ions in the plume. Therefore, a comparison of the beam divergence at differing magnetic fields is required.

Because the primary area of interest is the parametric effects of the discharge voltage and the magnetic field, current density is measured only for variations in these parameters. Example current density distributions at varying discharge voltages are shown in Fig. 21. Generally, as the discharge voltage increases, the intensity of the central peak increases. This reflects both an increase in overall beam current and a decrease in beam divergence. The increase in beam current is due to increased extraction of ions into the beam rather than the grids. The increased ion focusing is caused by the increased discharge voltage imparting greater axial kinetic energy into the ions and decreasing the radial velocity component relative to the total velocity. This results in a reduction of ions on the wings and an increase of ions in the center. This is more clearly illustrated in a semilog plot of the data from Fig. 21, shown in Fig. 22.

The overall effect on the beam divergence is best quantified by calculating the beam half-angle, plotted in Fig. 23. Increasing the discharge voltage decreases the beam half-angle as expected, but increasing the magnetic field also decreases the beam half-angle.

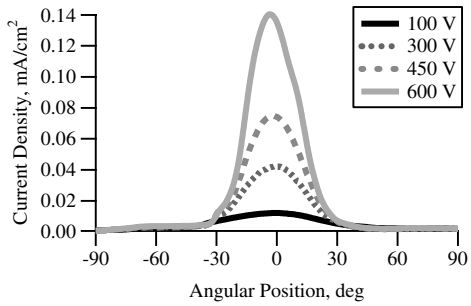

Fig. 21 Plume current density as function of discharge voltage 50 cm from grids; 429 W RF power, 150 G magnetic field, 1.5 mg/s argon, 35 V screen grid bias, 150 V accel grid bias, 1.6×10^{-5} torr Ar chamber pressure.

This suggests that the proposed mechanism of ambipolar electric fields creating a radial velocity component on the ion is either nonexistent, or the effect is negligible compared with another effect caused by increasing the magnetic field. One of the effects of increasing the magnetic field is increasing the discharge plasma density. This increases the perveance for an ion optics system that is already in overperveance. Increasing the perveance further would increase beam divergence, not reduce it. As a result, whatever mechanism is reducing the beam divergence does so in spite of competing phenomena.

D. Thrust

The thrust due to ion acceleration can be estimated in terms of the extracted beam current, the beam voltage V_b, and the beam divergence factor, as shown in Eq. (12):

$$T = I_b \gamma \sqrt{\frac{2 m_i V_b}{e}} \tag{12}$$

Values for the beam current and plume divergence factor are determined from the measured data, whereas the beam voltage can be approximated from the discharge voltage V_D and the cathode-to-ground voltage V_{ctg} [39]:

$$V_b \approx V_D - V_{\text{ctg}} \tag{13}$$

Figure 24 shows the estimated ion thrust using Eq. (12) as a function of magnetic field and discharge voltage.

To validate the estimates of ion thrust contribution, the thrust of the GHIT is measured directly for a sample set of operating conditions. The size of the sample set is limited due to the large uncertainty relative to the actual thrust measurements. The measured thrust sample is shown in Table 1 at the given operating conditions; parameters not listed in the table are constant between all tests: 600 V discharge, 35 V screen grid, and 150 V accel grid voltages. The measured thrust is slightly higher than the estimated thrust, because estimated thrust only considers thrust contributions from accelerated

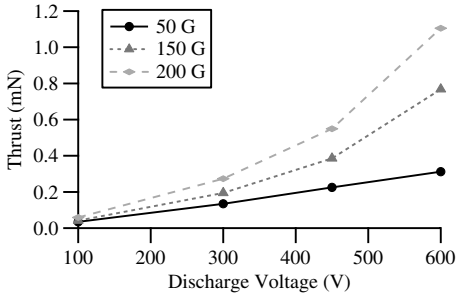

Fig. 24 Estimated thrust as function of discharge voltage and magnetic field; 429 W RF power, 1.5 mg/s argon, 35 V screen grid bias, 150 V accel grid bias, 1.6×10^{-5} torr Ar chamber pressure.

ions and does not include thrust from neutral gas pressure. Assuming a discharge pressure of 0.7 mtorr [43], thrust due to pressure is approximately 1.0 mN, which is approximately equal to the thrust discrepancy between the predicted and measured thrust. The calculated efficiency is on the order of that seen for a helicon plasma source alone, which is not unexpected considering the observed performance of the grid optics. Optimizing the grid geometry and voltages for the observed densities should greatly improve the efficiency of the device.

IV. Discussion

A. Discharge Chamber Analysis

The observed parametric effects on discharge performance were as expected. Increasing the magnetic field has such a strong impact on the ion density for two reasons: The first is that it decreases radial electron mobility and reduces electron losses to the walls. The second reason is that confinement of the electrons to gyrations along the magnetic field lines increases the overall path length traveled by an electron relative to axial distance traveled. This increases the probability that an electron will collide with a neutral before reaching the anode. Both of these mechanisms serve to increase ionization efficiency and the ion number density. Conversely, increasing the propellant flow rate increases neutral density and thus increases electron-neutral ionization collision frequency. However, the increased neutral density also increases ion-neutral neutralization collision frequency, as well as the frequency of electron-neutral collisions that increase radial electron mobility to the wall. Because of these competing effects, increasing the neutral pressure does not affect the discharge to the extent of a change in magnetic field.

The fact that the anode coil does not greatly increase ion density or temperature in the discharge is most likely due to the reliance on a magnetic mirror to restrict electron mobility to the anode [44]. The anode coil has such a small impact because collisions can alter the electron velocity and cause a confined electron to enter the loss cone. Inside the discharge, the mean free path of an electron is on the order of a centimeter, which means collisions are likely to mitigate the effectiveness of the anode coil.

B. Ion Optics

At all operating conditions, the accel grid current is considerably higher than desired for grid longevity. The minimum relative accel grid current observed is 0.23 at 600 W RF power, 50 G, 600 V discharge, and 1.5 mg/s. Figure 20 shows that, for all other operating conditions, the relative accel grid currents are higher. Using perveance to relate the grid voltages to the discharge plasma, the first cause for the high relative accel grid currents for most operating conditions is the relatively low potential drop across the grids compared with the ion current from the discharge plasma. As discharge voltage increases, the total potential drop between the screen and accel grids increases, which decreases the perveance. Because the relative accel grid current decreases as perveance decreases, the thruster is clearly operating in the overperveance condition. The expectation is that, as perveance is further decreased, the relative accel grid current would reach a minimum and then increase. This minimum would mark the optimum perveance of the grids for the given discharge plasma. However, this minimum is generally not observed, which indicates that further increases in the discharge voltage are required to reach optimum perveance. This increase in discharge voltage would reduce the relative accel grid current.

Table 1 Measured GHIT thrust and efficiency

P_{RF}, W	B, G	$\dot{m}_p$, mg/s	T, mN	I_{sp}, s	H, %
429	50	1.5	-0.13 ± 5.01	-8 ± 340	0.0013 ± 1.95
600	150	1.5	2.75 ± 2.00	187 ± 136	0.42 ± 0.22
429	200	1.5	2.77 ± 3.61	188 ± 245	0.60 ± 1.01
429	150	1.0	1.47 ± 2.19	150 ± 223	0.25 ± 0.56
429	150	2.0	2.28 ± 2.60	116 ± 133	0.30 ± 0.39
429	150	3.0	1.51 ± 2.35	51 ± 80	0.09 ± 0.21

Although optimal perveance is not reached in general, it is likely that optimal perveance is reached for the previously mentioned case at 600 W RF power, 50 G, 600 V discharge, and 1.5 mg/s. The last two discharge voltage points in Fig. 20, corresponding to 550 and 600 V, have nearly equal relative accel grid currents. This suggests that optimal perveance occurs either at 600 V, or very close to that value. However, this implies that, even at optimal perveance, the accel grid current is 23% of the ion beam current, which is still too high for long-term operation. This implies that a second cause for the high accel grid current exists, most likely the spatial variance of the discharge plasma density and temperature. The normalized perveance is an average over the entire grid assembly, which only gives the true perveance if the spatial distributions of the discharge plasma temperature and density are uniform. Because this is not the case, the normalized perveance is a spatial average of the perveance of each aperture. Thus, when the relative accel grid current as a function of the normalized perveance is minimized, rather than optimizing the perveance of every aperture individually, only a majority of the perveances is optimized. The nominal optimal perveance is thus a combination of apertures at optimal perveance and others at the condition of over- and underperveance. Therefore, uniform grids will always have a sizeable accel grid current when used with a spatially varying discharge plasma, even at the best perveance possible. The solution is to design the grids to include a spatial variance in aperture diameter to match the spatial variance in the discharge plasma temperature and density, such that optimal perveance is achieved simultaneously for as many apertures as possible.

A second indication of the grids not functioning as designed can be seen in Fig. 15. Despite the nontransparent portion of the screen grid only occupying 33% of the grid area, it collected 40% of the total ion flux. Ions are only extracted from the discharge through a plasma sheath from either the screen grid or the accel grid (neglecting ion losses to the discharge chamber wall). This shows that the screen grid sheath surface area accounts for 40% of the total sheath surface area, which is larger than the nontransparent grid area. This suggests that the accel grid sheath does not fully extend to the screen grid, which enables the screen grid sheath in the apertures to collect additional ions that would have passed through to the accel grid sheath. Figure 25 illustrates conceptually why severe overperveance would cause excessive screen grid ion collection.

This problem of the screen grid collecting ions in excess of expectations is a result of increased perveance. In terms of operating parameters, as the discharge density increases, the discharge voltage must be increased simply to maintain perveance. As the discharge density increases at constant grid voltage, the accel grid sheath length decreases and the accel grid sheath withdraws from the screen grid aperture. If the discharge density is progressively increased, the surface area of the accel grid sheath continues to decrease and the ratio of the screen grid current to the anode current increases. This effect is countered by an increase in the discharge voltage, which increases the sheath potential between the accel grid and the discharge plasma, thus increasing the sheath length and extending the accel grid sheath toward the screen grid. Figure 26 shows that these parametric effects hold: As discharge voltage is increased, the screen grid to anode current ratio decreases, representing a decrease in

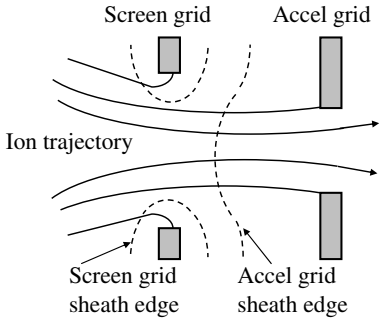

Fig. 25 Conceptualization of severe overperveance.

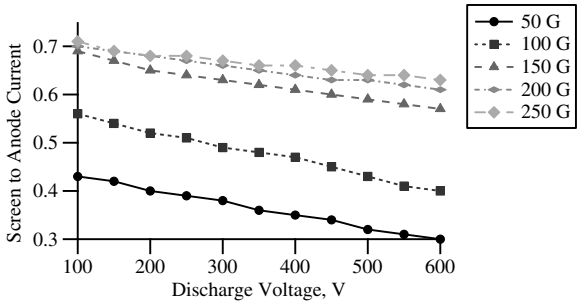

Fig. 26 Screen grid to anode current ratio as function of discharge voltage and magnetic field; 600 W RF power, 1.5 mg/s argon, 35 V screen grid bias, 150 V accel grid bias, 1.6×10^{-5} torr Ar chamber pressure.

screen grid collection and, by extension, an increase in accel grid sheath surface area. Increasing the magnetic field, which has already been found to increase discharge plasma density, increases the screen grid current collection relative to the anode. Furthermore, these data show that only the 50 G cases at higher discharge voltages came close to reaching optimal perveance, where the screen grid collected only about a third of the total ion flux. This demonstrates that future optimization of the GHIT will require higher discharge voltages at magnetic fields higher than 50 G to ensure proper accel grid sheath formation and optimal perveance.

The performance of the grid optics suggests two modifications to improve the GHIT. The first modification to the grid assembly would be to spatially match the aperture geometry to the discharge plasma characteristics. Assuming the discharge plasma is radially symmetric, the screen and accel grid aperture diameters would be a function of radial position. The second modification to the ion optics is to increase the potential drop across the grids, thereby decreasing the perveance for the same beam current. This will extend the accel grid sheath into the screen grid aperture and reduce screen grid collection of ions, as well as increase ion focusing and reduce ion impingement on the accel grid. As ion impingement on the grids decreased, this would increase the extracted beam current, which was the primary limitation to thrust. Higher beam current would then necessitate even higher discharge voltages to maintain perveance. At magnetic field strengths above 200 G, this would likely result in very large beam voltages and lower thrust-to-power ratios. Therefore, a further improvement would be to use a propellant with a larger atomic mass, such as krypton or xenon.

C. Plasma Source Utility

There are two key evaluations to make in determining the utility of a device modification: Does it provide a benefit, and does it create any additional problems that outweigh the benefits? In this particular instance, the comparison is between the cathode or RF discharges in state-of-the-art ion engines and the RF discharge in the GHIT. The benefit of using a nominal helicon discharge to generate ions is that it has the capability for a lower ion production cost than in state-of-the-art ion engine discharges, which increases efficiency [45]. One of the key improvements is the axial magnetic field, which provides radial confinement of the ions and reduces wall losses. Concurrently, the axial magnetic field does not adversely affect the ion optics. Rather, as observed, increasing the magnetic field strength decreases the beam half-angle despite the accompanying increase in overperveance. Therefore, the presented thruster, once the grids are properly optimized, offers comparable ion optics with a decrease in ion production cost compared with state-of-the-art ion engines.

V. Conclusions

A gridded helicon ion thruster has been fabricated and given an initial performance evaluation. Discharge ion density and electron temperature is found to range $1.5–9.3 \times 10^{16}$ m^{-3} and 5.4–9.9 eV, respectively, with a maximum beam current of 120 mA at a 600 V discharge. Maximum measured thrust is 2.77 mN. Beam current is primarily limited by ion collection by the screen and accel grids due to severe overperveance of the grids. Further ion losses are likely caused by spatial variation of the discharge chamber plasma, which creates a spatial variance of the perveance per aperture. Improvements in ion optics can be achieved by matching the grid apertures to the variation in the plasma density and increasing the voltage between the grids to decrease the perveance.

Acknowledgments

The authors would like to thank American Pacific in Space Propulsion for their support, the Georgia Tech Aerospace Engineering Machine Shop for fabrication and hardware support, as well as the students of the High-Power Electric Propulsion Laboratory for additional assistance. The authors would also like to thank Dan Goebel for assistance rendered in correspondence and conversation.

References

[1] Chen, F. F., "Plasma Ionization by Helicon Waves," *Plasma Physics and Controlled Fusion*, Vol. 33, No. 4, 1991, pp. 339–364. doi:10.1088/0741-3335/33/4/006

[2] Chen, F. F., "Helicon Plasma Sources," *High Density Plasma Sources*, edited by Popov, O. A., Noyes Publ., Park Ridge, NJ, 1995, pp. 1–75.

[3] Chen, F. F., "Experiments on Helicon Plasma Sources," *Journal of Vacuum Science and Technology*, Vol. 10, No. 4, 1992, pp. 1389–1401.

[4] Boswell, R. W., "Very Efficient Plasma Generation by Whistler Waves Near the Lower Hybrid Frequency," *Plasma Physics and Controlled Fusion*, Vol. 26, No. 10, 1984, pp. 1147–1162. doi:10.1088/0741-3335/26/10/001

[5] Degeling, A. W., Jung, D. O., Boswell, R. W., and Ellingboe, A. R., "Plasma Production from Helicon Waves," *Physics of Plasmas*, Vol. 3, No. 7, 1996, pp. 2788–2796. doi:10.1063/1.871712

[6] Perry, A. J., Vender, D., and Boswell, R. W., "Application of the Helicon Source to Plasma Processing," *Journal of Vacuum Science Technology*, Vol. 9, No. 2, 1991, pp. 310–317.

[7] Degeling, A. W., Sheridan, T. E., and Boswell, R. W., "Intense On-Axis Plasma Production and Associated Relaxation Oscillations in a Large Volume Helicon Source," *Physics of Plasmas*, Vol. 6, No. 9, 1999, pp. 3664–3673. doi:10.1063/1.873624

[8] Winglee, R., Ziemba, T., Giersch, L., Prager, J., Carscadden, J., and Roberson, B. R., "Simulation and Laboratory Validation of Magnetic Nozzle Effects for the High Power Helicon Thruster," *Physics of Plasmas*, Vol. 14, No. 6, 2007, Paper 063501. doi:10.1063/1.2734184

[9] Charles, C., "Review of Recent Laboratory Double Layer Experiments," *Plasma Sources Science and Technology*, Vol. 16, No. 4, 2007, pp. R1–R25. doi:10.1088/0963-0252/16/4/R01

[10] Charles, C., et al., "Helicon Double Layer Thrusters," *29th International Electric Propulsion Conference*, IEPC Paper 2005-290, 2005.

[11] Charles, C., Boswell, R. W., and Lieberman, M. A., "Xenon Ion Beam Characterization in a Helicon Double Layer Thruster," *Applied Physics Letters*, Vol. 89, No. 26, 2006, Paper 261503. doi:10.1063/1.2426881

[12] West, M. D., Charles, C., and Boswell, R. W., "Testing a Helicon Double Layer Thruster Immersed in a Space-Simulation Chamber," *Journal of Propulsion and Power*, Vol. 24, No. 1, 2008, pp. 134–141. doi:10.2514/1.31414

[13] Charles, C., and Boswell, R. W., "Current-Free Double-Layer Formation in a High-Density Helicon Discharge," *Applied Physics Letters*, Vol. 82, No. 9, 2003, pp. 1356–1358. doi:10.1063/1.1557319

[14] Cox, W., Charles, C., Boswell, R. W., and Hawkins, R., "Spatial Retarding Field Energy Analyzer Measurements Downstream of a Helicon Double Layer Plasma," *Applied Physics Letters*, Vol. 93, No. 7, 2008, Paper 071505. doi:10.1063/1.2965866

[15] Ling, J., West, M. D., Lafleur, T., Charles, C., and Boswell, R. W., "Thruster Measurements in a Low-Magnetic Field High-Density Mode in the Helicon Double Layer Thruster," *Journal of Physics D: Applied Physics*, Vol. 43, No. 30, 2010, Paper 305203. doi:10.1088/0022-3727/43/30/305203

[16] Takahashi, K., et al., "Direct Thrust Measurement of a Permanent Magnet Helicon Double Layer Thruster," *Applied Physics Letters*, Vol. 98, No. 14, 2011, Paper 141503. doi:10.1063/1.3577608

[17] Pottinger, S., Lappas, V., Charles, C., and Boswell, R., "Performance Characterization of a Helicon Double Layer Thruster Using Direct Thrust Measurements," *Journal of Applied Physics*, Vol. 44, No. 23, 2011, Paper 235201.

[18] Williams, L. T., and Walker, M. L. R., "Thrust Measurements of a Helicon Plasma Source," *AIAA/ASME/SAE/ASEE Joint Propulsion Conference & Exhibit*, AIAA Paper 2011-5893, 2011.

[19] Squire, J. P., et al., "VASIMR Performance Measurements at Powers Exceeding 50 kW and Lunar Robotic Mission Applications," *International Interdisciplinary Symposium of Gaseous Liquid Plasmas*, 2008.

[20] Longmier, B. W., et al., "Ambipolar Ion Acceleration in an Expanding Magnetic Nozzle," *Plasma Sources Science and Technology,* Vol. 20, No. 1, 2000, Paper 015007.

[21] Hwang, Y. S., Hong, I. S., and Eom, G. S., "Conceptual Design of a Helicon Ion Source for High-Current DC Accelerators," *Review of Scientific Instruments*, Vol. 69, No. 3, 1998, pp. 1344–1348.

[22] Mordyk, S., Miroshnichenko, V., Shulha, D., and Storizhko, V., "Investigation of Helicon Ion Source Extraction Systems," *Review of Scientific Instruments*, Vol. 79, No. 2, 2008, pp. 02B707–02B714.

[23] Hong, I. S., Hwang, Y. S., Lee, G. H., Kim, D. Y., Won, H. Y., Eom, G. S., and Choe, W., "Ion-beam Characteristics of Novel Helicon Ion Sources for Different Plasma Parameters," *Review of Scientific Instruments*, Vol. 71, No. 3, 2000, pp. 1385–1388. doi:10.1063/1.1150467

[24] Longmier, B., et al., "VX-200 Magnetoplasma Thruster Performance Results Exceeding Fifty-Percent Thruster Efficiency," *Journal of Propulsion and Power*, Vol. 27, No. 4, 2011, pp. 915–920. doi:10.2514/1.B34085

[25] Shabshelowitz, A., "Study of RF Plasma Technology Applied to Air-Breathing Electric Propulsion," Ph.D. Dissertation, Univ. of Michigan, Ann Arbor, MI, 2013.

[26] Brophy, J. R., et al., "Ion Propulsion System (NSTAR) DS1 Technology Validation Report," *DS1 Technology Validation Symposium*, 2000.

[27] Tsay, M. M., and Martinez-Sanchez, M., "Simple Performance Modeling of a Radio-Frequency Ion Thruster," *30th International Electric Propulsion Conference*, IEPC Paper 2007-072, 2007.

[28] Bassner, H., Killinger, R., Leiter, H., and Müller, J., "Development Steps of the RF-Ion Thrusters RIT," *27th International Electric Propulsion Conference*, IEPC 01-105, 2001.

[29] Groh, K. H., and Loebt, H. W., "State-of-the-Art of Radio-Frequency Ion Thrusters," *Journal of Propulsion and Power*, Vol. 7, No. 4, 1991, pp. 573–579. doi:10.2514/3.23364

[30] "MKS Product Specifications," *MKS 1179A Instruction Manual*, MKS Instruments, 2000, p. 57.

[31] Manzella, D. H., and Sankovic, J. M., "Hall Thrusters Ion Beam Characterization," *31st AIAA Joint Propulsion Conference*, AIAA Paper 1995-2927, 1995.

[32] Brown, D. L., "Investigation of Low Discharge Voltage Hall Thruster Characteristics and Evaluation of Loss Mechanisms," Ph.D. Dissertation, Univ. of Michigan, Ann Arbor, MI, 2009.

[33] Walker, M. L. R., Hofer, R. R., and Gallimore, A. D., "Effects of Nude Faraday Probe Design and Vacuum Facility Backpressure on the Measured Ion Current Density Profile of Hall Thruster Plumes," *38th AIAA Joint Propulsion Conference*, AIAA Paper 2002-4253, 2002.

[34] Hofer, R. R., Walker, M. L. R., and Gallimore, A. D., "Comparison of Nude and Collimated Faraday Probes for Use with Hall Thrusters," *27th International Electric Propulsion Conference*, IEPC 01-020, 2001.

[35] Mason, L. S., and Jankovsky, R. S., "1000 Hour of Testing on a 10 Kilowatt Hall Effect Thruster," *37th AIAA Joint Propulsion Conference*, AIAA Paper 2001-3773, 2001.

[36] Xu, K., "Ion Collimation and In-Channel Potential Shaping Using In-Channel Electrodes for Hall Effect Thrusters," Ph.D. Dissertation, Georgia Inst. of Technology, Atlanta, Georgia, 2012.

[37] Brown, D. L., and Gallimore, A. D., "Evaluation of Ion Collection Area in Faraday Probes," *Review of Scientific Instruments*, Vol. 81, No. 6, 2010, Paper 063504. doi:10.1063/1.3449541

[38] Xu, K. G., and Walker, M. L. R., "High-Power, Null-Type, Inverted Pendulum Thrust Stand," *Review of Scientific Instruments*, Vol. 80, No. 5, 2009, Paper 055103. doi:10.1063/1.3125626

[39] Goebel, D. M., and Katz, I., *Fundamentals of Electric Propulsion: Ion and Hall Thrusters*, edited by Yuen, J. H., Space Science and Technology Series, Jet Propulsion Lab., Pasadena, CA, 2008.

[40] Chen, F. F., "Plasma Ionization by Helicon Waves," *Plasma Physics and Controlled Fusion*, Vol. 33, No. 4, 1991, pp. 339–364. doi:10.1088/0741-3335/33/4/006

[41] Kaeppelin, V., Carrere, M., and Faure, J. B., "Different Operation Regimes in a Helicon Plasma Source," *Review of Scientific Instruments*, Vol. 72, No. 12, 2001, pp. 4377–4382. doi:10.1063/1.1419228

[42] Cos, W., Hawkins, R., Charles, C., and Boswell, R., "Three-Dimensional Mapping of Ion Density in a Double-Layer Helicon Plasma," *IEEE Transactions on Plasma Science*, Vol. 36, No. 4, 2008, pp. 1386–1387.

[43] Giannelli, S., Kieckhafer, A. W., and Walker, M. L. R., "Neutral Gas Expansion in a Cylindrical Helicon Discharge Chamber," *Journal of Propulsion and Power*, Vol. 29, No. 3, 2013, pp. 540–546.

[44] Chen, F. F., *Introduction to Plasma Physics and Controlled Fusion, Volume 1: Plasma Physics*, 2nd ed., Springer Science, New York, 2006, pp. 19–51.

[45] Williams, L. T., and Walker, M. L. R., "Ion Production Cost of a Gridded Helicon Ion Thruster," *Plasma Sources Science and Technology*, Vol. 22, No. 5, 2013, Paper 055019. doi:10.1088/0963-0252/22/5/055019

J. Blandino
Associate Editor